1

Using Synchrotron-Based X-Ray Microtomography and Functional Contrast Agents in Environmental Applications

Dorthe Wildenschild,* Mark L. Rivers, Mark L. Porter, Gabriel C. Iltis, Ryan T. Armstrong, and Yohan Davit

Abstract

Despite very rapid development in commercial X-ray tomography technology, synchrotron-based tomography facilities still have a number of advantages over conventional systems. The high photon flux inherent of synchrotron radiation sources allows for (i) high resolution to micro- or nanometer scales depending on the individual beam-line, (ii) rapid acquisition times that allow for collection of sufficient data for statistically significant results in a short amount of time as well as prevention of temporal changes that would take place during longer scan times, and (iii) optimal implementation of contrast agents that allow us to resolve features that would not be decipherable in scans obtained with a polychromatic radiation source. This chapter highlights recent advances in capabilities at synchrotron sources, as well as implementation of synchrotron-based computed microtomography (CMT) to two topics of interest to researchers in the soil science, hydrology, and environmental engineering fields, namely multiphase flow in porous media and characterization of biofilm architecture in porous media. In both examples, we make use of contrast agents and photoelectric edge-specific scanning (single- or dual-energy type), in combination with advanced image processing techniques.

Abbreviations: ALS, Advanced Light Source; APS, Advanced Photon Source; CAMD, Center for Advanced Microstructure and Devices; CCD, charge-coupled device; CLSM, confocal laser scanning microscopy; CMT, computed microtomography; CT, computed tomography; ESEM, environmental scanning electron microscopy; ESRF, European Synchrotron Radiation Facility; GSECARS, GeoSoilEnviroCARS; HASYLAB, Hamburger Synchrotronstrahlungslabor; ISA, ASTRID, Institute for Storage Ring Facilities; LuAG, lutetium–aluminum–garnet; MRM, magnetic resonance microscopy; NAPL, nonaqueous phase liquid; NSLS, National Synchrotron Light Source; REV, representative elementary volume; SLS, Swiss Light Source; S/N, signal-to-noise ratio.

D. Wildenschild, G.C. Iltis, and R.T. Armstrong, School of Chemical, Biological and Environmental Engineering, Oregon State Univ., Corvallis, OR 97331. M.L. Rivers, Dep. of Geophysical Sciences and Center for Advanced Radiation Sources, Univ. of Chicago, Chicago, IL 60637. M.L. Porter, Earth and Environmental Sciences Division, Los Alamos National Laboratory, Los Alamos, NM 87544. Y. Davit, Institut de Mecanique des Fluides de Toulouse, Univ. of Toulouse, France (now at Mathematical Institute, Univ. of Oxford, 24-29 St. Giles', Oxford OX1 3LB, UK). *Corresponding author (dorthe@engr.orst.edu).

doi:10.2136/sssaspecpub61.c1

Soil–Water–Root Processes: Advances in Tomography and Imaging. SSSA Special Publication 61. S.H. Anderson and J.W. Hopmans, editors.

The focus of this chapter is on X-ray *absorption* tomography (we do not cover X-ray fluorescence tomography or X-ray phase-contrast tomography). We describe various elements of the imaging process and present examples of how synchrotron radiation can be used with great advantage for characterizing many different variables of interest to the soil science, hydrologic, and environmental engineering communities. The synchrotron-based X-ray tomography section provides a brief introduction to synchrotrons and how X-rays interact with matter and also contains a discussion of how to optimize image quality via a discussion of resolution, contrast sensitivity, and artifacts. In the contrast agents section, we discuss contrast agents and the use of monochromators, while the image processing and analysis section provides a brief overview of some of the steps involved in image processing. Finally, the environmental applications section contains example applications where the use of synchrotron radiation and contrast agents has been crucial to success. We wish to emphasize that this entire chapter is meant more as a how-to guide than an extensive review of all the remarkable work that has been accomplished over the years with tomography—synchrotron-based or not. The two applications we focus on are based in work performed by this group of people and focuses on applications where we have found the use of monochromatic radiation to be essential. There are many other areas of research where great strides are being made using synchrotron-based microtomography, but a full review of these applications is beyond the scope of this text.

Synchrotron-Based X-Ray Tomography

A synchrotron light source is typically an electron storage ring that uses radio-frequency cavities to accelerate electrons to near the speed of light and magnetic fields to steer and focus the beam. When high-speed electrons are accelerated by the magnetic fields of a bending magnet, wiggler, or undulator, they emit electromagnetic radiation. The radiation spans an enormous range in wavelength and includes radio waves, visible light, and X-rays. The resulting synchrotron radiation is millions of times brighter than sunlight or laboratory X-ray tubes (see Fig. 1 in Kinney and Nichols, 1992).

Synchrotron sources can be divided into insertion devices (undulators and wigglers) and bending magnets, the main differences being in the spatial distribution and spectrum of light that is emitted. Undulators emit light that is highly collimated in both the vertical and horizontal directions (typically less than 0.05 mrad) and is in a narrow wavelength bandwidth. Bending magnets (and wigglers) emit a wide horizontal fan (several mrad), with a narrower vertical opening angle (0.1–0.3 mrad) and a continuous broad band of wavelengths. What all these sources have in common is very high emitted flux, and this is what renders synchrotron tomography such a powerful imaging tool. The wide bending magnet X-ray spectrum is most often monochromated into a narrow energy bandwidth, and this is a crucial feature, since it allows for energy specific imaging. Specifically, this permits the separation of features in the images using dual-energy (above and below the photoelectric edge) imaging (see the photoelectric edge enhancement and monochromators section for more on monochromators and edge enhancement). Tomography beam-lines based on bending magnets are

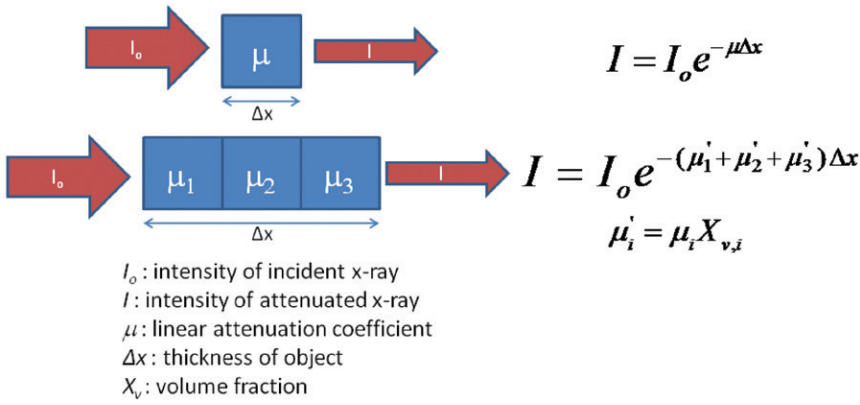

Fig. 1–1. X-ray attenuation of single and multi-component materials.

typically suitable for specimens in the 1- to 50-mm size range, while undulators are ideal for high-resolution images of samples under 2 mm in size.

X-Rays and Their Interaction with Matter

A synchrotron produces photons that can be used for a variety of analytical techniques and thus a very wide range of applications. Photons interacting with matter can be absorbed, scattered (elastic or inelastic), diffracted, or transmitted through the material. The absorption of photons can also stimulate emission of electrons, visible light, and X-rays. To better understand how to optimize tomographic imaging at synchrotrons, it is necessary to understand the basics of X-ray absorption (see Fig. 1–1).

Attenuation of X-rays as they pass through a solid object follows Lambert–Beer's law:

$$I = I_0 \exp(-\mu x) \qquad [1]$$

where I_0 is the incident monochromatic radiation intensity, I is the attenuated intensity after the X-rays have passed through an object of thickness x, and μ is the linear attenuation coefficient, which depends on the bulk, and thus electron density of the material, and the energy of the radiation. For low X-ray energies in the typical synchrotron beam-line range (~5–50 keV), X-rays interact with matter predominantly by photoelectric absorption, which is strongly dependent on atomic number, and this dependence is what allows us to use contrast agents to enhance contrast in many environmental applications as described in the contrast agents section. A more detailed description of X-ray attenuation and its relative dependence on these various components as a function of X-ray energy can be found in, for example, the papers by McCullough (1975) and Wildenschild et al. (2002). It can be seen from Eq. [1] that I is a decreasing function of distance, x, since the exponential argument ($\mu \Delta x$) is negative. This reflects the fact that the incident X-rays, I_0, are attenuated as they pass through an object, and this decrease has a characteristic length of $1/\mu$, called the attenuation length. This is the dis-

tance traveled by the X-rays before they are absorbed by 1/e, or about 63% (Margaritondo, 2002). Thus, materials with a high attenuation coefficient will allow X-rays to penetrate only a relatively short distance, whereas materials with a low attenuation coefficient will allow X-rays to travel farther through the material. There are a number of resources available on the internet by which one can evaluate the absorption properties of both elements and compounds for a wide range of energies: NIST XCOM Photon Cross-sections Database (http://www.nist.gov/pml/data/xcom/index.cfm) and the Center for X-ray Optics (http://www.cxro.lbl.gov/). The X-ray Data Booklet available from http://xdb.lbl.gov/ is also an invaluable resource.

From Eq. [1], we see that by measuring the incident intensity as well as $I(x)$, we can calculate the average linear attenuation coefficient of the (composite) material that the X-rays have passed through. Because attenuation coefficients for composite materials add linearly (see Fig. 1–1), we can also compute linear attenuation coefficients for the composite parts (μ') if we know the volume fractions, X_v. What is required for favorable imaging is sufficient variation in attenuation coefficients to accurately identify or classify objects or materials of different composition and density.

To perform tomography, it is necessary to collect projection (radiographic) images at a large number of angles, and these are then "reconstructed" into an image that reveals the details of the internal structure of the object. This reconstruction process is generally performed by a mathematical back-projection algorithm, a technique originally developed in 1917 by Johann Radon (later translated in Radon, 1986), who derived a method based on calculus by which one can unfold projection images from an object and from these projections recover the object itself (filtered back-projection).

Figure 1–2 illustrates how this would work for a pencil beam, and for the case of only four projections (which would generate a single two-dimensional slice). In three dimensions (and using a parallel beam), the object is similarly rotated and two-dimensional radiographic projections are collected at a large number of angles such that the full three-dimensional distribution of attenuation coefficients can be mathematically back-calculated, that is, reconstructed. If a sufficiently large number of projections (500–1000) are collected at different angles, typically over at least 180°, the optimization problem becomes sufficiently well-

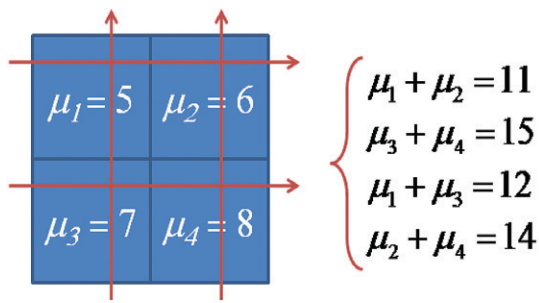

Fig. 1–2. Set of equations that needs to be solved for four projections, in this simplified case for four single ray paths, resulting in a two-dimensional slice of the object.

posed that it can be solved uniquely and with high accuracy, that is, producing a highly resolved three-dimensional distribution (image) of X-ray attenuation values. The rate of raw data generation from a synchrotron beam-line can exceed 10 Mb s^{-1}, and these data must be fairly rapidly normalized (to adjust for variation in white and dark currents), ordered into sinograms (all the projections put together to a volume makes up the sinogram), and then converted into image data during reconstruction. The typical back-projection reconstruction algorithm is an $O(N^3)$ problem, and with projections approaching 2000 by 2000 pixels, large computational resources are needed. Because it is possible to collect data 24 h a day, and at a very rapid rate, the amount of data generated is significant. A single reconstructed volume can vary in size from ~0.5 to 16 Gb depending on resolution, and during a typical 2- to 3-d run at the Advanced Photon Source (APS), we collect on the order of a quarter to half a terabyte of data. Processing, storing, and backing up these data locally require financial resources and incur network storage and administrative costs that are worth considering before starting a tomography-based project.

Synchrotron Facilities and Access

There are an increasing number of synchrotron radiation user facilities around the world; however, not all of these have beam-lines dedicated to X-ray tomography. Among the ones currently developed for tomography are the beam-lines at the

- Advanced Light Source (ALS) at Lawrence Berkeley National Laboratory, Berkeley, CA, USA
- Advanced Photon Source (APS) at Argonne National Laboratory, Argonne, IL, USA
- National Synchrotron Light Source (NSLS) at Brookhaven National Laboratory, Brookhaven, NY, USA
- Center for Advanced Microstructure and Devices (CAMD) at Louisiana State University, Baton Rouge, LA, USA
- European Synchrotron Radiation Facility (ESRF), Grenoble, France
- Swiss Light Source (SLS), Viligen, Switzerland
- Hamburger Synchrotronstrahlungslabor (HASYLAB) at DESY, Hamburg, Germany
- Diamond Light Source, Oxfordshire, United Kingdom
- Institute for Storage Ring Facilities (ISA, ASTRID), Aarhus, Denmark (energy range limited to image biological material only)
- MAX-LAB at Lund University, Lund, Sweden (proposed)
- Australian Synchrotron, Melbourne, Australia (commissioning)
- SPring-8 at Japan Synchrotron Radiation Research Institute, Hyogo, Japan
- Photon Factory, National Laboratory for High Energy Physics, Tsukuba, Japan
- Shanghai Synchrotron Radiation Facility, Shanghai, China

Most of these are run as user-facilities where individual users can apply for beam-time and, if successful, get access to the analytical equipment. An extensive review of the inner workings of an electron storage ring, the various types of synchrotrons (first to fourth generation), etc., is beyond the scope of this chapter and can be found in the works by Sham and Rivers (2002) and Margaritondo (2002), for example.

Experimental Constraints

A typical tomography beam-line setup is shown in Fig. 1–3. It generally involves an automated, micrometer-precision stage where the specimen is mounted and that can rotate through 360° as well as translate in three directions. After the X-rays have passed through the specimen, they strike a scintillator that converts the X-rays to visible light. At the GeoSoilEnviroCARS (GSECARS) bending magnet beam-line at the Advanced Photon Source (APS) at Argonne National Laboratory, the scintillator now consists of a single crystal lutetium–aluminum–garnet (LuAG) scintillation crystal. Various microscope objectives (or zoom and/or macro lenses) are then used to project the visible light onto a charge-coupled device (CCD) camera for image capture.

Depending on the brightness of the source, beam-line optics, and data collection parameters, acquisition times can be under 2 min per scan, but at some facilities, can also take hours, which bring the latter on par with modern polychromatic systems in terms of acquisition time. However, they still have the bright synchrotron light in common, which can be monochromated, and therefore used very favorably with contrast agents (see the contrast agents section), an approach that is not as optimally implemented when using a polychromatic radiation source. When choosing to perform research at a synchrotron facility, a potential user will therefore want to consider whether acquisition time is a constraint and which environmental settings can be accommodated (sample dimensions, vertical, and horizontal field of view, pressure and temperature control, etc.). Is equilibration time important for your experiment? Is it sensitive to temperature variations in the hutch?

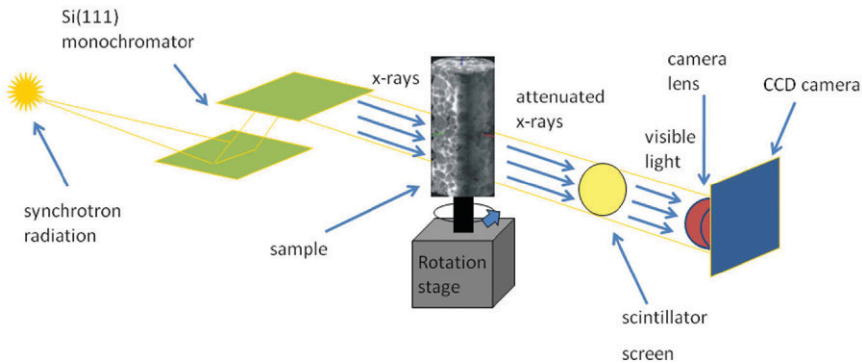

Fig. 1–3. Typical synchrotron tomography beam-line setup.

While the specific details of each microtomography beam-line may differ, all generally work roughly as described in the following which represents the setup at the GSECARS bending magnet beam-line (13 BMD).

The GSECARS bending magnet provides a fan beam of high-brilliance radiation, with an intrinsic vertical size of about 5 mm in the experimental station, about 55 m from the electron beam source point. When used with an Si [111] double-crystal monochromator, energies in the range from 7 to 65 keV can be obtained with a beam size up to 50-mm width and 5-mm height (Rivers et al., 1999). The stage setup facilitates automated translation and rotation of the object in the beam. Since the detector is two-dimensional, many slices (e.g., a complete three-dimensional data set) are obtained in a single 180° rotation (Fig. 1–3). After the X-rays are converted to visible light by the scintillator, they are imaged with a Nikon Macro lens, or 5×, 10×, or 20× Mitutoyo microscope objectives onto a high-speed 12-bit CCD camera (Photometrics CoolSnap HQ2), with 1392 by 1040 pixels, each 6.45 by 6.45 mm^2 in size. The raw data used for tomographic reconstruction are 12-bit images and a total of 720 to 1200 such images are typically collected as the sample is rotated from 0 to 180° in 0.25 to 0.15° steps. Reconstruction is accomplished either with filtered back-projection or the FFT-based Gridrec software, using the programming language IDL (Research Systems Inc.).

Resolution and Contrast

To obtain high-quality images, one must chose the X-ray energy such that there is 20 to 50% transmission through the more absorbing portions of the sample. This will result in good contrast and sufficient X-rays at the detector to obtain a good signal/noise (S/N) ratio. At the same time, the detector needs to have sufficient spatial resolution to discriminate between narrowly separated photon ray paths. High spatial resolution also depends on having a small source size, at a large distance, because source size contributes to image blur.

Compared to images obtained with many older conventional radiation sources, synchrotron-based tomography allows for superior resolution. However, polychromatic systems are developing rapidly, and it is now feasible to acquire data at similar resolutions with some of these newer systems, albeit using much longer acquisition times and generally with lower sensitivity to subtle attenuation differences. As a rule of thumb, the voxel resolution can be assumed to be approximately 1/1000 of the horizontal dimension of the specimen. This is mainly dictated by the field of view (sample size) divided by number of pixels of the detector (CCD camera), and the potential use of imaging optics. Resolution is also affected by the number of projections used, by S/N ratio (e.g., Stock, 1999), and by crystal resolution, scattering, and depth of field of the scintillator, the latter reducing it to 1 to 2 μm. Ultimately, resolution is constrained by the fact that the fundamental limit for a non-magnifying (parallel beam) technique is the diffraction limit for visible light, which is about 0.5 μm. For a non-parallel beam (i.e., cone or fan), the spot size of the source determines the physical limit of the resolution.

More recent developments using zone plates are capable of generating higher resolutions into the nanometer range, but for an increasingly small specimen size. It is worth noting that to obtain resolution on the order of nanometers, the specimen size needs to be so small that the chance of actually measuring REV (representative elementary volume)-appropriate flow and transport variables is diminishing.

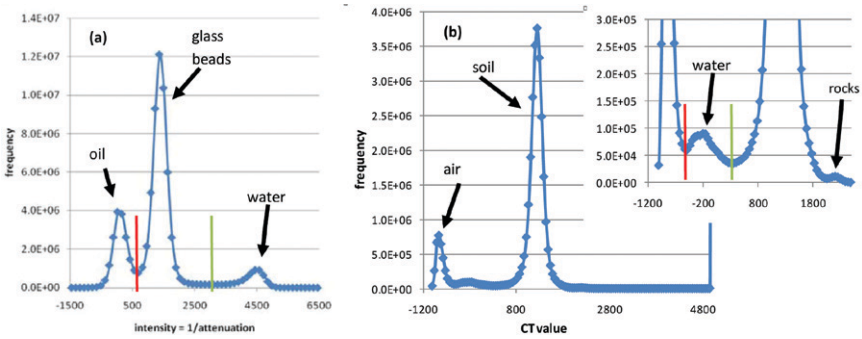

Fig. 1–4. (a) Synchrotron-based image of a partially saturated glass bead pack imaged at 10.8 μm. Using the new optics and lutetium–aluminum–garnet scintillator the different phases (oil, water, beads) are easily separated. (b) Typical medical computed-tomography (CT)-based histogram for a partially saturated clayey till soil column imaged at ~600 μm. Four different phases (air, water, soil, rocks) can be identified based on the histogram.

It should be noted here that for fine-grained soils, the resolution limit and resulting REV issue may become an issue for tomography at the micrometer resolution level as well because of the small scale heterogeneity and anisotropy of the pores.

Contrast is a measure of how well a feature can be distinguished from the surrounding background. It is often defined by the difference in attenuation between the feature and background, divided by the background attenuation. The ability to discriminate between two materials with closely similar linear attenuation values depends on the accuracy with which the values of μ, the linear attenuation coefficient, can be determined, and thus how well attenuation values for the phases of interest are separated (e.g., spatially in a histogram).

It should also be noted that there is a very large difference in what the human eye–brain cognitive unit can distinguish and what a computer can be programmed to automatically distinguish, especially for low-contrast objects.

Figure 1–4 shows example histograms for a partially saturated soil sample (20 cm tall by 20 cm in diameter), and a 7-mm diameter glass bead pack, partially saturated with water and oil. The samples were imaged with a medical CT (computed tomography) scanner at 600 μm resolution and with a synchrotron-based system at 10.8 μm resolution, respectively. It can be seen that the three phases of interest (solids, water, and air) can be distinguished in the histogram for the medical CT scan (Fig. 1–4b). Similar separation of features was also obtained using a tube X-ray microCT system (i.e., polychromatic radiation) by Tippköetter et al. (2009) so phase segmentation is straightforward and no contrast enhancement needed.

For data collected 10 yr ago with the synchrotron-based system, some of the different phases of interest would overlap, despite the use of a contrast agent; however, with recent upgrades of imaging optics and scintillator, the histograms are now similarly favorable (Fig. 1–4a) in terms of segmentation as those obtained for larger specimen size with medical CT or using a microCT system (see the experimental constraints and segmentation sections for further discussion of Fig. 1–4).

To optimize both spatial resolution and contrast sensitivity, it is necessary to select an X-ray energy that is appropriate for the material in question. The X-rays need to be sufficiently energetic to penetrate the sample, such that adequate counting statistics (S/N ratio) can be obtained. On the other hand, if the energy of the incoming radiation is too powerful, the relative attenuation will be low and the object becomes virtually transparent, with little or no contrast between the various phases.

Other Factors Affecting Image Quality

One of the advantages of (monochromatic) synchrotron radiation over polychromatic sources is that the images are not affected by beam-hardening artifacts. However, synchrotron sources are not free of ring artifacts, yet they can be minimized with careful correction algorithms in the data processing step. Ring artifacts are caused by local defects (drift and nonlinearities) in the scintillator or detection device, resulting in faulty low or high beam intensities, which then appear as rings in the reconstructed image. Furthermore, cosmic or scattered X-rays hitting the detector chip directly can cause anomalously bright pixels (zingers) and result in streak artifacts.

Other artifacts arise from movement in the object being imaged. If for instance, fluid interfaces in a porous medium are moving (equilibrating and redistributing) during the scan, a certain degree of blurring or streaking will result in the scanned image. The added "benefit" of this is that one can rather effectively ascertain whether quasi-equilibrium conditions have been achieved for the fluids involved. The term quasi-equilibrium is used here because minor adjustments in interface curvature may take longer and may not as readily show up as a motion artifact.

Partial-volume effects arise from the fact that a scanned object is often composed of a number of different substances, and the resulting discretized representation is therefore often an array of averaged values that cross interface boundaries. In other words, a scan of an object consisting of two different materials will likely produce a tomographic array of attenuation values that has a large fraction of voxels that can easily be classified as either material, but it will also have a number of voxels that have attenuation values that are fractional averages of the two materials. In addition, because of the inherent resolution limitations (of most imaging modalities), material boundaries are blurred to some extent, and the materials in a neighboring voxel may affect attenuation values in surrounding voxels.

All X-ray-based imagery is associated with some level of noise. In a perfect world, all voxel values for a uniform object should be identical; however, in reality, the voxel values are generally spread around a mean value. The magnitude of this variation is called image noise and arises because X-ray interaction and detection is a statistical process. Some noise can be successfully dealt with via image processing, but it is desirable to reduce the noise during image capture.

The time required to image a volume element or voxel with a certain statistical confidence increases drastically as the size of the voxel decreases. An object of smaller cross-section will absorb fewer photons and therefore requires longer exposure time to assure acceptable counting statistics. For instance, reducing the voxel size for a cube that is 100 μm on a side to 10 μm on a side will increase the exposure time by a factor of 10^4 (see Table 1 in Davis, 1999). Consequently, increasing spatial resolution requires larger incident photon intensity or longer

integration times. Synchrotron-based radiation is well suited for high resolution imaging because of the extremely high photon flux available. However, because it is difficult to produce energies above approximately 50 keV with synchrotron radiation sources, maximum sample size is generally limited to a few centimeters for specimens with composition and densities in the typical range of soil and rock samples so that the beam can penetrate the sample, whereas larger samples can be examined in conventional systems that generally use higher energies (e.g., Wildenschild et al., 2002).

Advantages and Limitations Relative to Polychromatic Radiation Sources

Synchrotron radiation has several advantages over traditional X-ray sources. These include the high intensity (number of photons per second) and thus rapid scan times, parallel beam geometry (which leads to more accurate reconstructions compared to cone-beam), no beam-hardening artifacts, and the ability to tune the photon energy over a wide range using a monochromator for obtaining optimal image contrast and element-specific measurements (Kinney and Nichols, 1992). The trade-off is in specimen size that can be imaged, and that the data is relatively noisy for small objects (low S/N ratio for micrometer-sized objects, unless longer exposure times are used): as discussed in the resolution and contrast section, high resolution does not dictate high contrast and easy segmentation. The histograms in Fig. 1–4 illustrate how it is possible to distinguish different phases in the medical CT data; however, only features that can be detected at 600 μm are captured. In the past, much smaller glass bead samples that were scanned with synchrotron radiation were significantly more noisy (e.g., Culligan et al., 2004) and thus the phases were not as easily distinguished. As mentioned earlier, recent advances in instrumentation has alleviated that problem, and regardless, the ability to optimally use contrast enhancement and dual-energy scanning which allow for generation of truly high-resolution images, where micrometer-scale features can be measured, far outweighs noise-related segmentation issues.

Contrast Agents

Photoelectric Edge Enhancement and Monochromators

In the range of energies that most synchrotrons operate at, X-rays interact with matter predominantly by photoelectric absorption, which strongly increases with atomic number (e.g., McCullough, 1975; Wildenschild et al., 2002). Absorption of X-rays occurs when an incoming X-ray photon is absorbed, resulting in the ejection of electrons from the inner shell of the atom, and the subsequent ionization of the atom. The ionized atom consequently returns to the neutral state (filling the vacated spot in the inner shell) often with the emission of an X-ray characteristic of the atom. The photoelectric effect can be used to great advantage to enhance the contrast of a phase (e.g., a fluid phase) that would otherwise have a very low X-ray cross-section (low absorption) and therefore not be easily distinguished in an X-ray tomographic image. By adding a contrast agent (dissolvable salt or suspension of a high atomic number element) to such a fluid phase (or otherwise adding it to the specimen of interest; see the environmental applications

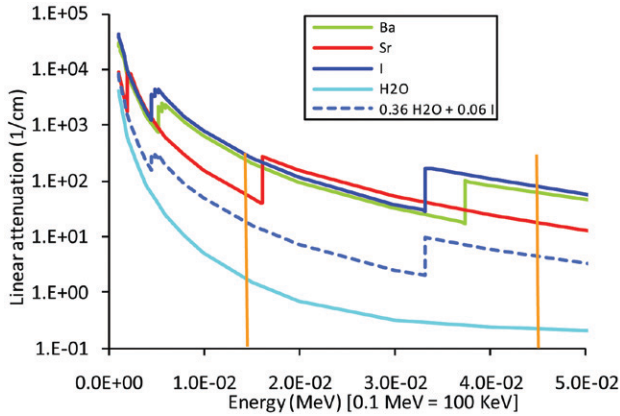

Fig. 1–5. Linear attenuation as a function of energy for select elements of interest in tomographic imaging. The curve for water and a 1:6 mixture of water and KI is also shown. The vertical orange bars depict the (15–45 keV) range of energies that it is feasible to use for soil and rock samples of ∼5-mm diameter.

section), it is possible to enhance the contrast of this fluid phase, if the energy of the incident X-rays is tuned to enhance the absorption of the contrast agent.

As mentioned previously, bending magnet beam-lines are often used with a tunable monochromator that can be used to select a narrow energy band from the white synchrotron light. Following Bragg's law, each constituent wavelength that is directed at a single crystal of known orientation and d-spacing (also known as the interatomic spacing) will be diffracted at a discrete angle.

Monochromators make use of the Bragg relationship to selectively pass only the radiation of interest, that is, in a narrow tunable band of interest. The radiation outside of this energy range is thus removed. Because of the high photon flux of synchrotrons, the flux after this monochromatization is still sufficient for fast and high-resolution imaging, whereas a similar procedure would render a conventional radiation source rather depleted and result in very long scan times and very noisy images. Figure 1–5 shows the attenuation as a function of energy for several commonly used contrast agents (Ba, Sr, and I), as well as the attenuation for water, and for a 1:6 mass ratio of water and potassium iodide.

The abrupt increases in attenuation represent the point where the incoming X-rays exceeded the photoelectric (K-shell edge) energy for the element or compound of interest. From this figure, it is evident that two images collected immediately above and below the edge will result in very different absorption, and the two images can be subtracted to clearly bring out the phase that contains the element (or compound) of interest. The range of energies that can realistically be achieved at a synchrotron, and that will allow for penetration (and adequate counts) of a approximately 0.5-cm diameter object with the density of a soil or rock sample (~15–45 keV) is indicated by orange bars on the figure. As the sample thickness increases, it is necessary to use higher photon energies, and thus contrast agents (elements) in the higher energy range.

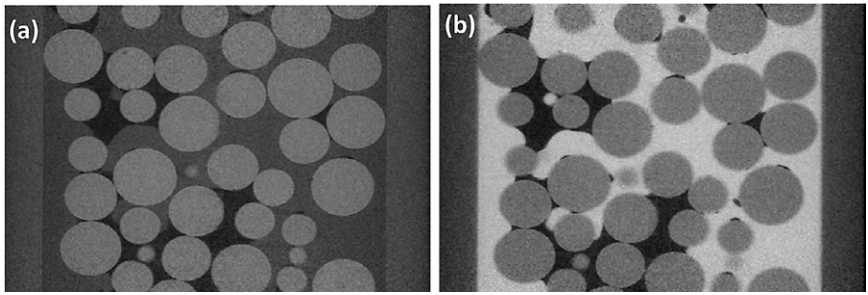

Fig. 1–6. (a) Below the Cs edge image; (b) The same image above the Cs edge.

Traditional Dissolved and Functionalized Contrast Agents

The photoelectric effect has been used to great advantage in X-ray tomography studies for decades; however, it can be optimally exploited using synchrotron-based systems. Among the contrast agents most commonly used are dissolved solutions of compounds such as KI, NaI, CsCl, RuCl, and iodized organics such as iodoheptane, iodobenzene, and iodononane. These compounds are, for instance, added to the fluid of interest (e.g., water or oil) in percentages necessary to produce good contrast (generally in the few-percent range). It is then fairly straightforward to tune the energy of the incident radiation to the relevant edge and produce images with high absorption in the doped fluid phase. The potential impact of the dopant on fluid properties and behavior can be a concern. Initial examination of this issue indicated no measurable impact of the dopant on measured properties (saturation, blob volumes, and surface areas) for the systems investigated by Schnaar and Brusseau (2005). This issue should be examined for each application of interest. Figure 1–6 shows images obtained with energies below and above the Cs-edge, respectively. When comparing the two images, the photoelectric effect is obvious. If two fluids need to be separated in the resulting images, two different contrast agents can be used, and scans can be performed above each element-specific edge to allow for subsequent subtraction, which then brings out the separate phases. This is useful when studying three-phase-fluid systems where an organic, a water, and a gas phase need separation and quantification (Brown et al., 2011).

In addition to the more traditionally used dissolved contrast agents, other means of achieving contrast can also be implemented as illustrated by the example provided below on imaging biofilms in porous media. Key to the process is to choose contrast agents that speciate, dissolve, attach, adsorb, or are excluded from the phase of interest.

Image Processing and Analysis

Ideally, tomographic images would be easy to segment into the desired phases of interest, but generally a number of processing steps of varying difficulty need to be accomplished to arrive at that point. As a general rule, it is much easier to obtain good image quality by optimizing the process at the point of capture, so adjusting the settings (energy level, exposure time, number of projections, etc.)

before starting a scan is well worth one's time. As described above, much can also be done at the point of image capture with respect to contrast enhancement using energy selective dopants. This drastically simplifies the amount of processing needed, and is often necessary to generate quantitative results that are accurate enough to draw technically reliable conclusions. A few of the most common aspects of image processing are described in the following section; however, several of these steps can be fairly complex and deserve attention beyond the scope of this chapter.

Pixelation and Discretization Effects

All images consist of pixilated versions of reality and no matter how good a resolution one can achieve, that is ultimately the case. That said, higher resolution will obviously produce more reliable quantification of small features, but also at the cost of the size of the imaged region, and therefore REV. Use of numerical models similarly force us to discretize the world we wish to investigate, and one can argue quite strongly that a discretized version of pore-scale phenomena is better than no characterization.

Registration

In many quantitative applications, it is desirable to be able to track a specimen as it goes through some sort of alteration, such as changing fluid saturations, precipitates forming or dissolving, or colloids attaching to an interface. For this purpose, it is necessary to register all the images to the same coordinate system. This can be accomplished quite readily because most beam-lines are equipped with very accurate rotation and translation stages that can be adjusted to below micrometer resolution. If for some reason the object has moved, there are now many types of commercial (and some free) software available that provide algorithms for auto-registration.

Segmentation

Following a close second to optimal image capture, segmentation (also often referred to as thresholding or binarization) is the most important step in producing high-quality results from a scan. If sufficient effort has been made to generate data with good contrast and high resolution, segmentation can be achieved using simple histogram thresholding. Two examples were shown in Fig. 1–4 that illustrate the relative ease with which thresholding can be performed when the different phases of interest have well-separated attenuation values; the two segmentation thresholds are indicated by the red and green vertical lines. However, even if a histogram looks less favorable than the ones in Fig. 1–4, it is often possible, using a number of segmentation steps, to generate good quantitative results. In a situation where the solid and water phases overlap, a simple approach is to scan the dry porous medium and then, relying on perfect registration, subtract the "dry" image from the partially saturated image (e.g., Culligan et al., 2004). A number of approaches also exist for handling more complex segmentation problems, such as the watershed segmentation approach (e.g., Sheppard et al., 2004), K-means cluster analysis (e.g., Porter and Wildenschild, 2009), and indicator kriging (e.g., Oh and Lindquist, 1999), the latter incorporating spatial information through the two-point covariance of the image. A full description of the many

different types of segmentation algorithms is beyond the scope of this chapter; we refer to Iassonov et al. (2009) for a detailed overview of segmentation techniques. In summary, much more attention has been paid to the extraction of pore network, porosity, mineral phases, etc. than to extracting information about fluid phases, interfacial characteristics, and their evolution. A number of segmentation algorithms and processing steps leading to estimates of interfacial area from tomographic images were tested by Porter and Wildenschild (2009) to assess their accuracy against measured values. The particular geometries were fluid–fluid interfaces (menisci) in capillary tubes of varying sizes that were imaged with microtomography. Most of the algorithms, except for two-point correlation functions and voxel counting approaches, produced estimates that were between 2 and 15% of the actual values. In general, one can assume that the more complex the scheme, the more computationally intensive it is.

Phase Quantification and Distribution

Once the image is segmented, the data analysis can commence. Some of the simpler measurements that can be made from tomographic images are sample porosity, fluid saturations and their spatial distributions, classification of pores into matrix and macropores, etc. Porosity and saturation can be estimated by simply counting the number of voxels assigned to each phase during segmentation. In many cases, medial-axis based network generating algorithms such as 3DMA Rock (Lindquist, 1999; Lindquist and Venkatarangan, 1999; Prodanović et al., 2006) are used to produce statistical representations of the imaged pore space for use in numerical network models. More recently (e.g., Lehmann et al., 2006; Vogel et al., 2010), mathematical morphology and Minkowski functionals have also been employed to quantify various properties of the porous medium, such as pore volume (porosity), surface area, curvature, and the Euler characteristic, which quantifies the connectivity of a porous medium.

Surface Generation and Curvature Estimation

For more complex variables such as solid surface area, fluid–fluid interfacial area, and curvature, it is highly recommended to use more sophisticated surface generating techniques such as the commonly implemented marching cubes algorithm (Lorensen and Cline, 1987), as opposed to using voxel-counting techniques. The marching cubes technique is a high-resolution three-dimensional surface construction algorithm that produces a triangle mesh by computing isosurfaces from discrete data. By connecting the patches from all cubes on the isosurface boundary, a surface representation is produced. From this surface, it is possible to measure variables such as surface area and fluid–fluid interfacial area (e.g., Porter and Wildenschild, 2009), and by approximating the surface locally by a quadratic polynomial (and using the principal curvatures at the point on the graph of such a quadratic polynomial as the approximation of the principal curvatures at the original surface point), interfacial curvature can be calculated (Armstrong et al., 2012; Armstrong and Wildenschild, 2012).

Environmental Applications

Multiphase Flow

In the following section, the term multiphase shall refer to both air-water and oil-water fluid systems in porous media. Computed microtomographic (CMT) imaging has been widely used in the fields of soil science, hydrology, petroleum engineering, and environmental engineering. In petroleum engineering, the focus has often been on extraction of porosity, pore morphology, network information, and relative permeability estimates for use in pore network simulators (e.g., Coles et al., 1998; Lindquist and Venkatarangan, 1999; Turner et al., 2004; Prodanović et al., 2007), whereas in soils and hydrology research, more work has focused on multiphase variables and on estimating properties such as fluid saturation and distribution (e.g., Clausnitzer and Hopmans, 1999, 2000; Perret et al., 2000); on describing soil structural features such as macropores (e.g., Anderson et al., 1990; Peth et al., 2008; Luo et al., 2010), root structure (e.g., Kaestner et al., 2006; Tracy et al., 2010), and plant uptake mechanisms (e.g., Scheckel et al., 2007). We refer to Taina et al. (2008) for an extensive review of tomography applications in soil science, and to Werth et al. (2010) for contaminant hydrology-type applications. In environmental engineering, *synchrotron*-based microtomography has been widely used to describe multiphase variables such as nonaqueous phase liquid (NAPL) characteristics (blob morphology, e.g., Al-Raoush and Willson, 2005a, 2005b; Schnaar and Brusseau, 2005, 2006) and on measuring multiphase variables such as fluid saturations and distribution (e.g., Wildenschild et al., 2005), fluid–fluid specific interfacial area (e.g., Culligan et al., 2004, 2006; Brusseau et al., 2006, 2007; Costanza-Robinson et al., 2008; Porter et al., 2009, 2010) and curvatures (Armstrong et al., 2012).

While porosities and fluid saturations are relatively easy to obtain with conventional sources, the more recent measurements of variables such as fluid–fluid interfacial area and curvature could not have been accomplished without the use of synchrotron beam-lines, either because of insufficient resolution and/or contrast, but also because of the rapid acquisition times that allow for collection of sufficient data for statistically significant results in a short amount of time. The rapid scan times also prevent temporal changes that would take place during scans with longer acquisition time. These capabilities have, for instance, allowed for concurrent measurement of capillary pressure (P_c), saturation (S), and fluid–fluid interfacial area (a_{nw}), a relationship that has received much attention in recent years as researchers are trying to generate data in support of new thermodynamics-based theories of multiphase flow.

Hassanizadeh and Gray (1993) expanded the traditional functional dependence of the P_c–S relationship to include a_{nw}, which explicitly accounts for the numerous fluid–fluid interfacial configurations that may exist for any given saturation value. In addition, Hassanizadeh and Gray (1993) hypothesized that the inclusion of a_{nw} in the macroscale formulation of P_c would account for hysteresis observed in the traditional P_c–S relationship. In recent work using synchrotron-based measurements of P_c–S–a_{nw} and lattice-Boltzmann simulations, Porter et al. (2009) were able to show that this appears to be the case because they found that hysteresis was virtually nonexistent in the P_c–S–a_{nw} relationship as opposed to the hysteretic P_c–S plane.

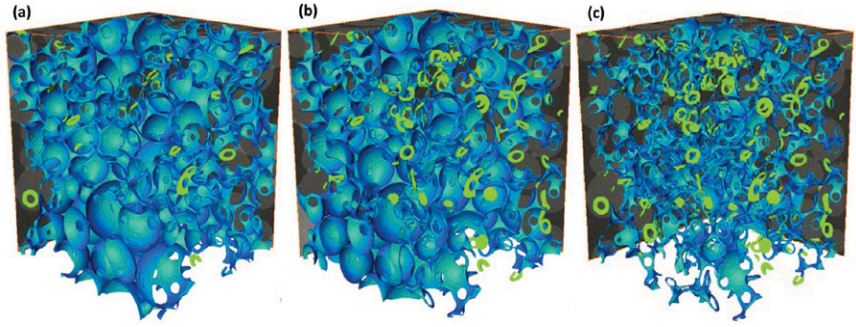

Fig. 1–7. Computed microtomography image of glass bead pack with continuous wetting phase (blue) and isolated pendular rings (green). Solid and gas phases have been removed. Image resolution is 13.0 μm and the imaged region is 5.5 mm tall. (a) drainage S_w = 0.38 (b) imbibition S_w = 0.37 (c) imbibition S_w = 0.09.

Similarly, high-resolution imaging has also provided tools that allow us to better understand how fluid phases and interfaces evolve as saturation and capillary pressures change—for instance as illustrated in Fig. 1–7. In this particular sequence of images, we are able to observe how the wetting phase (blue) is disconnected and left behind as pendular rings (green) as the sample changes saturation, and those disconnected pendular rings are then subsequently absorbed into the bulk wetting fluid on imbibition. The images also illustrate the significant difference in fluid distribution during drainage (Fig. 1–7a) and imbibition (Fig. 1–7b) at similar saturations (connected + disconnected). Additionally, the images illustrate that even at the low wetting fluid saturation of 9% there is still connected fluid from top to bottom of the imaged region.

The availability of multiphase data sets with this type of pore-scale detail has also allowed for detailed comparison and evaluation of various types of numerical models (pore network models, lattice-Boltzmann, pore morphology-based), for instance by Vogel et al. (2005), Schaap et al. (2007), Joekar-Niasar et al. (2007, 2010), Sukop et al. (2008), and Porter et al. (2009).

Biofilm Architecture

Imaging biofilms in porous media without disturbing the natural spatial arrangement of the porous medium and associated biofilm is challenging, primarily because porous media generally precludes conventional imaging. Conventional techniques for imaging biofilm include light microscopy (e.g., Yang et al., 2000; Sharp et al., 2005), environmental scanning electron microscopy (ESEM) (e.g., Davis et al., 2009), and confocal laser scanning microscopy (CLSM) (e.g., Leis et al., 2005; Rodriguez and Bishop, 2007), all of which are useful for examining biofilm on surfaces or in two-dimensional or quasi-two-dimensional porous systems. Imaging porous-media-associated biofilm using these techniques requires that model porous media systems either be constrained to a few particle diameters, that the porous medium and fluid be index-matched, or that samples be extracted and prepared, thereby disrupting the pore scale structure (Iltis et al., 2011). Thus, new techniques that allow for direct visualization of biofilm in situ are required to characterize biofilm surface architecture, and spatial distribu-

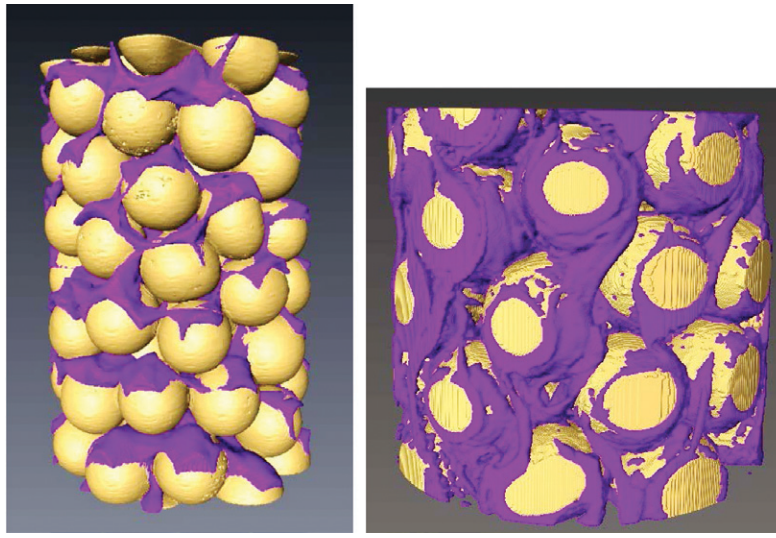

Fig. 1–8. (a) Glass bead pack (yellow) with biofilm (purple) delineated using the strained Ag particle approach (*Deinococcus radiodurans* imaged at 9.8 μm); (b) Glass bead pack (yellow) with biofilm (purple) delineated using the $BaSO_4$ suspension approach (*Escherichia coli* imaged at 11.3 μm). Flow is upward in both experiments.

tion within porous media. One such three-dimensional technique is magnetic resonance microscopy (MRM) (e.g., Seymour et al., 2004, 2007). Yet, thus far, the method has been limited in resolution (resolving features on the order of 50–100 μm), and acquisition time is significant.

Synchrotron-based X-ray tomography offers a potential alternative because it renders the solid phase transparent. The main obstacle to using X-rays for biofilm visualization and characterization is the fact that biofilms and their aqueous environment have very similar X-ray absorption capacities and are therefore difficult to separate in a reliable and quantitative manner. To overcome this problem, two different approaches have been developed based on novel use of X-ray contrast agents. At this point, we have tested two different techniques:

(i) Physical straining or adhesion of an X-ray contrast agent on the outer surface of the biofilm, and

(ii) Physical separation of biofilm and aqueous solution based on size-exclusion of a suspension of an X-ray contrast agent.

Examples of biofilm geometries imaged with each of these two approaches are shown in Fig. 1–8. For the first approach, silver-coated hollow glass microspheres were added to the fluid phase to function as an X-ray contrast that does not diffuse into the biofilm mass, but attaches to the outer surface of the biofilm. Using this approach, biofilm imaging in porous media was accomplished with sufficient contrast to differentiate between the biomass- and fluid–filled pore spaces (see Fig. 1–8a). The method was validated by using both light microscopy and CMT imaging to image biofilm in a two-dimensional micromodel flow

cell by Iltis et al. (2011). Additional work is required to optimize this imaging approach; specifically, we find that the quality of the images are highly dependent on the coverage of the biofilm by the dopant microspheres, which could be problematic for dead-end pore space and for very low density biofilms. This technique is, however, particularly well-suited for outlining the biofilm surface that is well-connected to flow paths and thus well-supplied with nutrients and active in transformation. The second approach is based on use of a $BaSO_4$ suspension, which functions as a very good X-ray contrast agent and is size-excluded from entering the biofilm (see Davit et al., 2011). Using a commercially available, polychromatic tomography system and packs of polystyrene beads as their porous medium, Davit et al. (2011) used a second aqueous phase dopant (KI) which also diffused into the biofilm to help separate the low-contrast (polystyrene) beads from the other phases. Before imaging, the aqueous solution was replaced with the $BaSO_4$ suspension to effectively separate the two phases of interest (aqueous phase via Ba contrast and biofilm phase via I contrast) from the polystyrene beads. This approach obviously lends itself very nicely to implementation using a synchrotron-based system because of the edge-specific imaging that the monochromatic light allows for. In addition, we have found that when using glass beads as the solid phase, it is not necessary to use the second dopant since the solid phase (glass beads) and proxy aqueous phase (the $BaSO_4$ suspension) uniquely defines the biofilm as the remaining phase once these other two are delineated (see Fig. 1–8b).

Conclusions

X-ray tomography has been used for many decades now to generate three-dimensional information about geological, biological, and manufactured objects of interest. A large number of commercial systems have been developed over the years, and along with those many very capable software programs (both commercial and freeware) that can perform almost any type of analysis, regardless of complexity. The days of having to write processing algorithms from scratch when analyzing the accompanying large (and ever-growing) volumes of data are fortunately over, as long as one can afford the not insignificant cost involved in purchasing such software or if one has the resources to learn how to use some of the excellent freeware programs.

The availability of synchrotron-based tomography to a general population of users has brought about tremendous gains in knowledge in a vast number of fields, not the least in the petroleum engineering, hydrologic, soil science, and environmental engineering areas of research. Data obtained with synchrotron-based microtomography has helped advance our understanding of how pore-scale mechanisms and interactions take place, and has established a platform for evaluation of how pore-scale processes affect continuum-scale flow, transport, and transformation. The availability of detailed pore-scale information has helped, and will continue to help, advance pore-scale modeling efforts by providing realistic input information against which numerical models can be tested.

New developments in instrumentation and data acquisition speeds, such as new CMOS cameras which can be run at very high speeds, up to 1200 frames per s for 2048 by 2048 cameras, allow an entire three-dimensional dataset to be collected in under 1 s. When used with filtered white beam from a bending magnet, it will

allow for dynamic imaging. Similarly, the rapidly evolving field of phase contrast tomography will likely also open up new avenues of exploration—in particular in areas where materials with low X-ray attenuation are of interest, but where differences in refractive index can be taken advantage of, say for imaging biological materials in a harder surrounding matrix (e.g., biofilms in porous media).

Acknowledgments

This work was supported by NSF-EAR-06101108 and NSF-EAR-0337711. A portion of this work was conducted at GeoSoilEnviroCARS (Sector 13), Advanced Photon Source (APS), Argonne National Laboratory. GeoSoilEnviroCARS is supported by the National Science Foundation-Earth Sciences (EAR-0622171) and Department of Energy-Geosciences (DE-FG02-94ER14466). Use of the Advanced Photon Source was supported by the U.S. Department of Energy, Office of Science, Office of Basic Energy Sciences, under contract DE-AC02-06CH11357. We thank the entire staff at GSECARS for experimental support. This work was also partially supported by the Environmental Remediation Science Program (DE-FG02-09ER64734) under the Department of Energy, Office of Biological and Environmental Research (BER), grant ER64734-1032845-0014978. Some of the work was also performed at Beam-line 8.3.2 at the Advanced Light Source (ALS), LBNL.

References

Al-Raoush, R.I., and C.S. Wilson. 2005a. Extraction of physically realistic pore network properties from three-dimensional synchrotron x-ray microtomography images of unconsolidated porous media systems. J. Hydrol. 300:44–64. doi:10.1016/j.jhydrol.2004.05.005

Al-Raoush, R.I., and C.S. Wilson. 2005b. A pore-scale investigation of a multiphase porous media system. J. Contam. Hydrol. 77:67–89. doi:10.1016/j.jconhyd.2004.12.001

Anderson, S.H., R.L. Peyton, and C.J. Gantzer. 1990. Evaluation of constructed and natural soil macropores using X-ray computed tomography. Geoderma 46:13–29. doi:10.1016/0016-7061(90)90004-S

Armstrong, R.T., M.L. Porter, and D. Wildenschild. 2012. Linking pore-scale interfacial curvature to column-scale capillary pressure. Adv. Water Resour.46:55–62.

Armstrong, R.T., and D. Wildenschild. 2012. Microbial enhanced oil recovery in fractional-wet systems: A pore-scale investigation. Transp. Porous Media 92:819–835.doi: 10.1007/s11242-011-9934-3

Brown, K.I., D. Wildenschild, W.G. Gray, and C.T. Miller. 2011. Interfacial area measurements for robust models of multiphase flow in porous media. Proceedings of the 2011 Goldschmidt Conference, August 14–19, 2011, Prague, Czech Republic, abstract.

Brusseau, M.L., S. Peng, G. Schnaar, and M.S. Costanza-Robinson. 2006. Relationship among air–water interfacial area, capillary pressure and water saturation for a sandy porous medium. Water Resour. Res. 42:W03501. doi:10.1029/2005WR004058

Brusseau, M.L., S. Peng, G. Schnaar, and A. Murao. 2007. Measuring air–water interfacial areas with X-ray microtomography and interfacial partitioning tracer tests. Environ. Sci. Technol. 41:1956–1961. doi:10.1021/es061474m

Clausnitzer, V., and J.W. Hopmans. 1999. Determination of phase volume fractions from tomographic measurements in two-phase systems. Adv. Water Resour. 22:577–584. doi:10.1016/S0309-1708(98)00040-2

Clausnitzer, V., and J.W. Hopmans. 2000. Pore-scale measurements of solute breakthrough using microfocus X-ray tomography. Water Resour. Res. 36:2067–2079. doi:10.1029/2000WR900076

Coles, M.E., R.D. Hazlett, P. Spanne, W.E. Soll, E.L. Muegge, and K.W. Jones. 1998. Pore level imaging of fluid transport using synchrotron X-ray microtomography. J. Petrol. Sci. Eng. 19:55–63. doi:10.1016/S0920-4105(97)00035-1

Costanza-Robinson, M.S., K.H. Harrold, and R.M. Lieb-Lappen. 2008. X-ray microtomography determination of air–water interfacial area-water saturation relationships in sandy porous media. Environ. Sci. Technol. 42:2949–2956. doi:10.1021/es072080d

Culligan, K.A., D. Wildenschild, B.S. Christensen, W.G. Gray, and M.L. Rivers. 2006. Pore-scale characteristics of multiphase flow in porous media: A comparison of air–water and oil–water experiments. Adv. Water Resour. 29:227–238. doi:10.1016/j.advwatres.2005.03.021

Culligan, K.A., D. Wildenschild, B.S. Christensen, W.G. Gray, M.L. Rivers, and A.B. Tompson. 2004. Interfacial area measurements for unsaturated flow through porous media. Water Resour. Res. 40:W12413. doi:10.1029/2004WR003278

Davis, D., L. Pyrak-Nolte, E. Atekwana, and D. Werkema. 2009. Microbial- induced heterogeneity in the relationship among acoustic properties of porous media. Geophys. Res. Lett. 36:L21405. doi:10.1029/2009GL039569

Davis, G.R. 1999. Image quality and accuracy in X-ray microtomography. Proc. SPIE Dev. X-ray Tomogr. 3772:147.doi:10.1117/12.363716

Davit, Y., G. Iltis, G. Debenesta, S. Veran-Tissoiresa, D. Wildenschild, M. Gerinoc, and M. Quintard. 2011. Imaging biofilms in porous media using X-ray computed microtomography. J. Microsc. 242:15–25.doi: 10.1111/j.1365-2818.2010.03432.x

Hassanizadeh, S.M., and W.G. Gray. 1993. Thermodynamic basis of capillary pressure, saturation, interfacial area and relative permeability using in porous media. Water Resour. Res. 29:3389–3405.

Iassonov, P., T. Gebrenegus, and M. Tuller. 2009. Segmentation of X-ray computed tomography images of porous materials: A crucial step for characterization and quantitative analysis of pore-network modeling. Transp. structures. Water Resour. Res. 45:W09415. doi:10.1029/2009WR008087

Iltis, G., R.T. Armstrong, D.P. Jansik, B.D. Wood, and D. Wildenschild. 2011. Imaging biofilm architecture within porous media using synchrotron-based X-ray computed microtomography. Water Resour. Res. 47:W02601.doi: 10.1029/2010WR009410

Joekar-Niasar, V., S.M. Hassanizadeh, and A. Leijnse. 2007. Insights into the relationships among capillary pressure, saturation, interfacial area and relative permeability using pore-network modeling. Porous Med. 74(2): 201–19. doi:10.1007/s11242-007-9191-7

Joekar-Niasar, V., M. Prodanovic, D. Wildenschild, and S.M. Hassanizadeh. 2010. Network model investigation of interfacial area, capillary pressure and saturation relationships in granular porous media. Water Resour. Res. 46:W06526. doi:10.1029/2009WR008585

Kaestner, A., M. Schneebeli, and F. Graf. 2006. Visualizing three-dimensional root networks using computed tomography. Geoderma 136:459–469. doi:10.1016/j.geoderma.2006.04.009

Kinney, J.H., and M.C. Nichols. 1992. X-ray tomographic microscopy (XTM) using synchrotron radiation. Annu. Rev. Mater. Sci. 22:121–152. doi:10.1146/annurev.ms.22.080192.001005

Lehmann, P., P. Wyss, A. Flisch, E. Lehmann, P. Vontobel, M. Krafczyk, A. Kaestner, F. Beckmann, A. Gygi, and H. Flühler. 2006. Tomographical imaging and mathematical description of porous media used for the prediction of fluid distribution. Vadose Zone J. 5:80–97. doi:10.2136/vzj2004.0177

Leis, A.P., S. Schlicher, H. Franke, and M. Strathmann. 2005. Optically transparent porous medium for nondestructive studies of microbial biofilm architecture and transport dynamics. Appl. Environ. Microbiol. 71(8):4801–4808. doi:10.1128/AEM.71.8.4801-4808.2005

Lindquist, W., and A. Venkatarangan. 1999. Investigating 3d geometry of porous media from high resolution images. Phys. Chem. Earth 25(7):593–599.

Lindquist, W.B. 1999. 3DMA-Rock, A Software Package for Automated Analysis of Pore Rock Structure in 3D Computed Microtomography Images; http://www.ams.sunysb.edu/~lindquis/3dma/3dma_rock/3dma_rock.html.

Lorensen, W.E., and H.E. Cline. 1987. Marching cubes: A high resolution 3D surface construction algorithm. Comput. Graph. 21:163–169. doi:10.1145/41997.41999

Luo, L., H. Lin, and S. Li. 2010. Quantification of 3-D soil macropore networks in different soil types and land uses using computed microtomography. J. Hydrol. 393:53–64. doi:10.1016/j.jhydrol.2010.03.031

Margaritondo, G. 2002. Elements of synchrotron light for biology, chemistry, and medical research. Oxford Univ. Press, Oxford, UK.

McCullough, E.C. 1975. Photon attenuation in computed tomography. Med. Phys. 2:307–320. doi:10.1118/1.594199

Oh, W., and B. Lindquist. 1999. Image thresholding by indicator kriging. IEEE Trans. Pattern Anal. Mach. Intell. 21(7):590–602. doi:10.1109/34.777370

Perret, J., S.O. Prasher, A. Kantzas, and C. Langford. 2000. A two-domain approach using CAT scanning to model solute transport in soil. J. Environ. Qual. 29:995–1010. doi:10.2134/jeq2000.00472425002900030039x

Peth, S., R. Horn, F. Beckmann, T. Donath, J. Fischer, and A.J.M. Smucker. 2008. Three-dimensional quantification of intra-aggregate pore-space features using synchrotron-radiation-based microtomography. Soil Sci. Soc. Am. J. 72:897–907. doi:10.2136/sssaj2007.0130

Porter, M.L., M.G. Schaap, and D. Wildenschild. 2009. Comparison of interfacial area estimates for multiphase flow through porous media using computed microtomography and lattice-boltzmann simulations. Adv. Water Resour. 32:1632–1640.doi:10.1016/j.advwatres.2009.08.009, Advances in Water Resources.

Porter, M.L., and D. Wildenschild. 2009. Validation of an image analysis method for computed microtomography image data of multiphase flow in porous systems. Comput. Geosci. 14:15–30.doi:10.1007/s10596-009-9130-5

Porter, M.L., D. Wildenschild, G. Grant, and J.I. Gerhard. 2010. Measurement and prediction of the relationship between capillary pressure, saturation, and interfacial area in a NAPL-water-glass bead system. Water Resour. Res. 46:W08512. doi:10.1029/2009WR007786

Prodanović, M., W.B. Lindquist, and R.S. Seright. 2006. Porous structure and fluid partitioning in polyethylene cores from 3D X-ray microtomographic imaging. J. Colloid Interface Sci., 298, 282–297.

Prodanović, M., W.B. Lindquist, and R. Seright. 2007. 3d image-based characterization of fluid displacement in Berea core. Adv. Water Resour. 30:214–226. doi:10.1016/j.advwatres.2005.05.015

Radon, J. 1986. On the determination of functions from their integral values along certain manifolds. IEEE Trans. Med. Imaging 5(4):170–176. doi:10.1109/TMI.1986.4307775

Rivers, M.L., S.R. Sutton, and P. Eng. 1999. Geoscience applications of X-ray computed microtomography. Proceedings of the SPIE Conference on Developments in X-ray Tomography II, July 1999, Denver, CO. p. 78–86.

Rodriguez, S.J., and P.L. Bishop. 2007. Three-dimensional quantification of soil biofilms using image analysis. Environ. Eng. Sci. 24(1):96–103. doi:10.1089/ees.2007.24.96

Schaap, M.G., M.L. Porter, B.S.B. Christensen, and D. Wildenschild. 2007. Comparison of pressure-saturation characteristics derived from computed tomography and Lattice Boltzmann simulations. Water Resour. Res. 43:W12S06. doi:10.1029/2006WR005730

Scheckel, K.G., R. Hamon, L. Jassogne, M. Rivers, and E. Lombi. 2007. Synchrotron X-ray absorption-edge computed microtomography imaging of thallium compartmentalization. Plant Soil 290:51–60.doi:10.1007/s11104-006-9102-7

Schnaar, G., and M.L. Brusseau. 2005. Pore-scale characterization of organic immiscible-liquid morphology in natural porous media using synchrotron X-ray microtomography. Environ. Sci. Technol. 39:8403–8410. doi:10.1021/es0508370

Schnaar, G., and M.L. Brusseau. 2006. Characterizing pore-scale configuration of organic immiscible liquid in multi-phase systems using synchrotron X-ray microtomography. Vadose Zone J. 5:641–648. doi:10.2136/vzj2005.0063

Seymour, J.D., J.P. Gage, S.L. Codd, and R. Gerlach. 2004. Anomalous fluid transport in porous media induced by biofilm growth. Phys. Rev. Lett. 93(19):198103. doi:10.1103/PhysRevLett.93.198103

Seymour, J.D., J.P. Gage, S.L. Codd, and R. Gerlach. 2007. Magnetic resonance microscopy of biofouling induced scale dependent transport in porous media. Adv. Water Resour. 30(6–7):1408–1420. doi:10.1016/j.advwatres.2006.05.029

Sham, T.K., and M.L. Rivers. 2002. A brief overview of synchrotron radiation. In: P.A. Fenter et al., editors, Reviews in mineralogy and geochemistry, Vol. 49: Applications of synchrotron radiation in low-temperature geochemistry and environmental science. Mineralogical Society of America, Chantilly, VA. p. 117–148.

Sharp, R.R., P. Stoodley, M. Adgie, R. Gerlach, and A. Cunningham. 2005. Visualization and characterization of dynamic patterns of flow, growth and activity of biofilms growing in porous media. Water Sci. Technol. 52(7):85–90

Sheppard, A.P., R.M. Sok, and H. Averdunk. 2004. Techniques for image enhancement and segmentation of tomographic images of porous materials. Phys. A 339:145–151. doi: 0.1016/j.physa.2004.03.057

Stock, S.R. 1999. X-ray microtomography of materials. Int. Mater. Rev. 44:141–164. doi:10.1179/095066099101528261

Sukop, M.C., H. Huang, C.L. Lin, M.D. Deo, K. Oh, and J.D. Miller. 2008. Distribution of multiphase fluids in porous media: Comparison between lattice Boltzmann modeling and micro-x-ray tomography. Phys. Rev. E Stat. Nonlin. Soft Matter Phys. 77:026710. doi:10.1103/PhysRevE.77.026710

Taina, I.A., R.J. Heck, and T.R. Elliot. 2008. Application of X-ray computed tomography to soil science: A literature review. Can. J. Soil Sci. 88:1–20. doi:10.4141/CJSS06027

Tippkötter, R., T. Eickhorst, H. Taubner, B. Gredner, and G. Rademaker. 2009. Detection of soil water in macropores of undisturbed soil using microfocus X-ray tube computerized tomography (mCT). Soil Tillage Res. 105:12–20. doi:10.1016/j.still.2009.05.001

Tracy, S.R., J.A. Roberts, C.R. Black, R. Colin, A. McNeill, R. Davidson, and S.J. Mooney. 2010. The X-factor: Visualizing undisturbed root architecture in soils using X-ray computed tomography. J. Exp. Bot. 61:311–313. doi:10.1093/jxb/erp386

Turner, M., L. Knüfing, C. Arns, A. Sakellariou, T. Senden, A. Sheppard, R. Sok, A. Limaye, W. Pinczewski, and M. Knackstedt. 2004. Three-dimensional imaging of multiphase flow in porous media. Physica A 339:166–172. doi:10.1016/j.physa.2004.03.059

Vogel, H.-J., J. Tölke, V. Schulz, M. Krafczyk, and K. Roth. 2005. Comparison of a lattice-Boltzmann model, a full-morphology model, and a pore network model for determining capillary pressure–saturation relationships. Vadose Zone J. 4:380–388. doi:10.2136/vzj2004.0114

Vogel, H.-J., U. Weller, and S. Schlüter. 2010. Quantification of soil structure based on Minkowski functions. Comput. Geosci. 36:1236–1245. doi:10.1016/j.cageo.2010.03.007

Werth, C.J., C. Zhang, M.L. Brusseau, M. Oostrom, and T. Baumann. 2010. A review of non-invasive imaging methods and applications in contaminant hydrogeology research. J. Contam. Hydrol. 113(1–4):1–24. doi:10.1016/j.jconhyd.2010.01.001

Wildenschild, D., J.W. Hopmans, A.J.R. Kent, and M.L. Rivers. 2005. A quantitative study of flow-rate dependent processes using X-ray microtomography. Vadose Zone J. 4:112–126. doi:10.2113/4.1.112

Wildenschild, D., J.W. Hopmans, C.M.P. Vaz, M.L. Rivers, and D. Rikard. 2002. Using X-ray computed tomography in hydrology: Systems, resolutions, and limitations. J. Hydrol. 267(3–4):285–297. doi:10.1016/S0022-1694(02)00157-9

Yang, X.M., H. Beyenal, G. Harkin, and Z. Lewandowski. 2000. Quantifying biofilm structure using image analysis. J. Microbiol. Methods 39(2):109–119. doi:10.1016/S0167-7012(99)00097-4